

# The influence of front strength on the development and equilibration of symmetric instability. Part 1. Growth & saturation

A. F. Wienkers<sup>1</sup>, L. N. Thomas<sup>2</sup> and J. R. Taylor<sup>1†</sup>

<sup>1</sup>Department of Applied Mathematics and Theoretical Physics, University of Cambridge, Centre for Mathematical Sciences, Wilberforce Road, Cambridge CB3 0WA, UK

<sup>2</sup>Department of Earth System Science, Stanford University, Stanford, CA 94305, USA

(Received xx; revised xx; accepted xx)

Submesoscale fronts with large horizontal buoyancy gradients and  $\mathcal{O}(1)$  Rossby numbers are common in the upper ocean. These fronts are associated with large vertical transport and are hotspots for biological activity. Submesoscale fronts are susceptible to symmetric instability (SI) — a form of stratified inertial instability which can occur when the potential vorticity is of the opposite sign to the Coriolis parameter. Here, we use a weakly nonlinear stability analysis to study SI in an idealised frontal zone with a uniform horizontal buoyancy gradient in thermal wind balance. We find that the structure and energetics of SI strongly depend on the front strength, defined as the ratio of the horizontal buoyancy gradient to the square of the Coriolis frequency. Vertically bounded non-hydrostatic SI modes can grow by extracting potential or kinetic energy from the balanced front and the relative importance of these energy reservoirs depends on the front strength and vertical stratification. We describe two limiting behaviours as ‘slantwise convection’ and ‘slantwise inertial instability’ where the largest energy source is the buoyancy flux and geostrophic shear production, respectively. The growing linear SI modes eventually break down through a secondary shear instability, and in the process transport considerable geostrophic momentum. The resulting breakdown of thermal wind balance generates vertically-sheared inertial oscillations and we estimate the amplitude of these oscillations from the stability analysis. We finally discuss broader implications of these results in the context of current parameterisations of SI.

**Key words:**

---

## 1. Introduction

The upper ocean is a dynamically active and important region, relevant not only to Earth’s climate due to exchanges at the air-sea interface, but to biogeochemical processes. Turbulence acts to vertically-homogenise this upper-most layer of the ocean down to typical depths of 10 to 100 metres, driven by wind stresses, surface waves, heat or salinity fluxes, or internal flow instabilities. Dynamics in the mixed layer influence exchanges of heat, momentum, carbon, oxygen, and other important biogeochemical tracers with the ocean interior.

Fronts, or regions with large lateral density gradients, are common in the upper ocean.

† Email address for correspondence: J.R.Taylor@damtp.cam.ac.uk

38 These lateral gradients of the background density field,  $\bar{\rho}$  (measured by the horizontal  
 39 analogue to the buoyancy frequency,  $M^2 \equiv g/\rho_0 |\nabla_h \bar{\rho}|$ , with  $g$  the acceleration due to  
 40 gravity, and  $\rho_0$  a reference density) are often in near-geostrophic balance and may be  
 41 generated by the frontogenetic strains of mesoscale eddies, by coastal upwelling, intrusions  
 42 into intermediate waters, or river discharges. Additionally, persistent frontal systems in  
 43 the ocean include western boundary currents (e.g. the Gulf Stream and Kuroshio) and  
 44 the Antarctic Circumpolar Current.

45 Horizontal density gradients can drive across-front flow due to baroclinic torques,  
 46  $g/\rho_0 \nabla_h \bar{\rho} \times \hat{\mathbf{z}}$  (where  $\hat{\mathbf{z}}$  is the vertical unit vector). These baroclinic torques tend to  
 47 flatten isopycnals, but may be counterbalanced by a Coriolis torque,  $f \partial_z \bar{\mathbf{u}}_g$  (where  $f$  is  
 48 the Coriolis parameter), arising from a vertical shear in the geostrophic velocity,  $\bar{\mathbf{u}}_g$ . This  
 49 geostrophic balance with the horizontal gradient of hydrostatic pressure arising from the  
 50 background density field is often called the thermal wind balance. The reservoir of poten-  
 51 tial energy associated with the horizontal density gradient and kinetic energy associated  
 52 with the thermal wind is available to energise secondary motions. The dynamics within  
 53 fronts (if not the entirety of frontal systems), however, are often unresolved in global  
 54 and regional numerical models. A better understanding of these self-regulating frontal  
 55 dynamics is therefore crucial to modelling the up-scale influence of unresolved processes.

56 Fronts are susceptible to a number of linear instabilities which drive submesoscale  
 57 (100m - 10km) motions. Baroclinic instability releases the potential energy stored in the  
 58 horizontal density gradient, rather than extracting it from the thermal wind shear (Char-  
 59 ney 1947; Stone 1972), and is a major mechanism behind the generation of submesoscale  
 60 eddies (e.g. Boccaletti *et al.* 2007; Fox-Kemper *et al.* 2008; Callies *et al.* 2016). Symmetric  
 61 Instability (SI) is an ageostrophic instability that can develop in frontal regions when  
 62 the Ertel potential vorticity (PV)

$$q \equiv (f \hat{\mathbf{z}} + \nabla \times \mathbf{u}) \cdot \nabla b, \quad (1.1)$$

63 (defined with the velocity,  $\mathbf{u}$ , and buoyancy,  $b \equiv -g\rho/\rho_0$ ) is of the opposite sign to the  
 64 Coriolis parameter,  $f$  (Hoskins 1974). The destabilising contributions of a balanced flow  
 65 are evident if we decompose the PV into a vortical and baroclinic component, respectively

$$q = (\omega_z + f) N^2 - M^4/f, \quad (1.2)$$

66 where  $\omega_z$  is the vertical component of the relative vorticity and  $M^2 \equiv \partial_x \bar{b}$  (as above) is  
 67 the horizontal analogue to the buoyancy frequency,  $N^2 \equiv \partial_z \bar{b}$ . A negative PV does not  
 68 necessarily imply SI, however. In the absence of a frontal buoyancy gradient (i.e.  $M^2 = 0$ )  
 69 ‘gravitational instability’ occurs when  $N^2 < 0$  and  $\omega_z + f > 0$  whereas ‘inertial instability’  
 70 occurs when  $N^2 > 0$  and  $\omega_z + f < 0$ . Therefore SI only occurs when  $(\omega_z + f) N^2 > 0$   
 71 but  $M^4/f$  is sufficiently large so that  $f q < 0$ . Much of the ocean interior is sufficiently  
 72 stratified such that  $f q > 0$ . However, as noted by Thomas *et al.* (2016), a frictional stress  
 73 or diabatic flux at the surface and bottom boundaries lead to  $f q < 0$  and trigger SI.

74 In the context of the Eady model with uniform horizontal and vertical buoyancy  
 75 gradients, Stone (1966) found that symmetric modes, defined as those independent of the  
 76 along-front direction (i.e. perpendicular to the horizontal buoyancy gradient), grow faster  
 77 than baroclinic modes (independent of the cross-front direction) for  $Ri < 0.95$ , where  
 78  $Ri \equiv N^2 f^2 / M^4$  is the balanced Richardson number. Stone (1971) considered the non-  
 79 hydrostatic contributions to symmetric and baroclinic instabilities in the ageostrophic  
 80 Eady model, showing that the vertical inertia suppresses both baroclinic and symmetric  
 81 instabilities. Viscous contributions to the bounded non-hydrostatic SI problem were  
 82 then included by Weber (1980) and approximated by a viscosity acting on a vertically-  
 83 unbounded normal mode. Beyond the Eady model other types of instability are possible.

84 For example, Wang *et al.* (2014) describe a variety of instabilities that develop in  
 85 more general vertically-sheared flows and how they relate to symmetric and baroclinic  
 86 instability in the Eady model.

87 Recent observational studies have accumulated evidence of SI in the ocean. For exam-  
 88 ple, increased turbulence and dissipation (exceeding that from atmospheric forcing) in  
 89 regions where  $fq < 0$  has been attributed to SI (Thomas *et al.* (2016) in the Gulf Stream,  
 90 and D’Asaro *et al.* (2011) in the Kuroshio). This negative PV is generated by atmospheric  
 91 forcing — either by upward buoyancy fluxes (for example cooling) (Haine & Marshall  
 92 1998; Thomas *et al.* 2013) or wind-stresses (Thomas & Lee 2005) — which can reduce the  
 93 PV, and sustain ‘SI turbulence’ and mixing stronger than what the forcing alone could  
 94 generate. Thompson *et al.* (2016*b*) and later Yu *et al.* (2019) have also found evidence  
 95 for SI in glider and mooring observations of the open ocean away from major frontal  
 96 systems. Recently, Savelyev *et al.* (2018) captured aerial images of SI in the North Wall  
 97 of the Gulf Stream (cf. fig. 2), which constitutes the only visual evidence of the structure  
 98 of SI to date.

99 Vertically-sheared inertial oscillations of the isopycnals can result from the rapid  
 100 mixing of geostrophic momentum, and were present following the saturation of SI in  
 101 the simulations of Taylor & Ferrari (2009). Tandon & Garrett (1994) modelled the  
 102 response of a mixed layer front to impulsive vertical mixing using the inviscid hydrostatic  
 103 equations. After a mixing event, the front undergoes inertial oscillations and modulates  
 104 the background stratification about the average steady-state position ( $Ri = 1$ ). Tandon  
 105 & Garrett (1994) also considered the case when the vertical stratification is perfectly  
 106 homogenised (for example by a passing storm), but where the geostrophic shear is  
 107 partially mixed leaving only a fraction,  $s$ , of the balanced shear profile. We will show  
 108 that when acting on times short relative to the inertial period, then SI can generate  
 109 sufficient geostrophic momentum transport needed to prompt adjustment. We quantify  
 110 this mixing fraction,  $(1 - s)$ , resulting from the effects of SI.

111 A number of previous numerical process studies of SI have investigated its nonlinear  
 112 evolution with varying setups, but most have focused only on a single value of the non-  
 113 dimensional horizontal buoyancy gradient (Thomas & Lee 2005; Taylor & Ferrari 2009;  
 114 Thomas & Taylor 2010; Taylor & Ferrari 2010; Stamper & Taylor 2016). Nonetheless,  
 115 between persistent fronts, transient fronts, and mid-ocean fronts, the strength of these  
 116 horizontal buoyancy gradients span a large range in the ocean (Hoskins & Bretherton  
 117 1972; Jinadasa *et al.* 2016; Thompson *et al.* 2016*a*). We therefore vary the front strength,  
 118  $\Gamma \equiv M^2/f^2$ , rather than changing the vertical stratification as measured by  $Ri$ .

119 In this paper, we investigate the equilibration of SI-unstable fronts. We focus on the  
 120 development and saturation of SI in the Eady model configuration to determine the  
 121 transport by SI and explain how the rate of energy extraction and amplitude of the  
 122 resulting inertial oscillations vary with frontal strength. To do this, we first extend the  
 123 non-hydrostatic and bounded linear analysis of Stone (1971) to include viscosity. We  
 124 represent the vertical viscous terms using the wave-mode approximation of Weber (1980)  
 125 to find an analytic solution, but further solve the full numerical eigensystem to verify this  
 126 approximation in the regime of interest. Compared to Stone (1966) and ensuing papers  
 127 which studied instability of the Eady model in the inviscid, hydrostatic limit, our analysis  
 128 is no longer a function only of  $Ri$ , but now also depends on the front strength,  $\Gamma$ .

129 These purely linear analyses are unable to determine the finite contribution of SI to  
 130 the momentum transport, buoyancy fluxes, and energetics of the flow. We analyse the  
 131 weakly-nonlinear problem by considering the growth of secondary instabilities on the  
 132 growing finite-amplitude SI modes. Our analysis formally extends the work by Taylor &  
 133 Ferrari (2009) who implicitly considered the secondary shear instability of (unbounded)

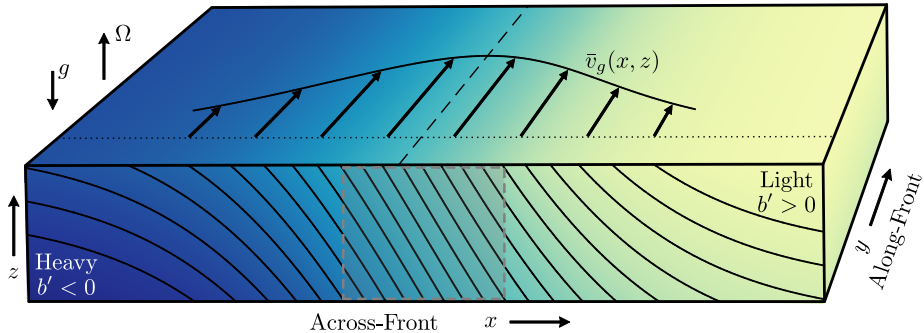


FIGURE 1. Schematic of a model frontal region showing coloured contours of density varying both across the front and vertically. The across-front stratification is balanced by the thermal wind shear in  $\bar{v}_g$ , shown on the top face. A local horizontally-homogeneous model can be constructed by considering the region within the grey box, where the buoyancy gradient is approximately uniform.

134 SI modes by applying the Miles-Howard theorem. We are thereby able to compute a  
 135 critical amplitude beyond which SI transitions to turbulence and calculate the efficiency  
 136 with which SI mixes geostrophic momentum prior to transition. To our knowledge this is  
 137 the first calculation of the mixing fraction,  $(1 - s)$ , (as used by Tandon & Garrett (1994)  
 138 to describe the geostrophic response of a front) associated with symmetric instability.

139 We begin in §2 by introducing the problem set-up and primary linear stability analysis  
 140 for SI. In §2.3, we consider the stability of these growing SI modes to secondary shear  
 141 instability and find a critical mode amplitude beyond which the front transitions to  
 142 turbulence. We finally combine these two stability analyses in §4 and §5 to determine  
 143 the finite-amplitude contributions of SI to the energetics and momentum transport,  
 144 respectively.

145 In a companion paper, we explore the nonlinear consequences of these findings beyond  
 146 the saturation point. We extend the numerical simulations (from §3 here used for  
 147 validation) to study the evolution of these fronts following SI. We use the framework  
 148 of Tandon & Garrett (1994) to shed light on the effects of dissipation and a finite mixing  
 149 time on the adjustment response and resulting inertial oscillations.

## 150 2. Linear stability analysis

151 Perhaps the simplest model of a front, the Eady model was first introduced by Eady  
 152 (1949) and later used by Stone (1966) and Stone (1970) to study ageostrophic instabilities.  
 153 As illustrated in figure 1, the Eady model can be viewed as a local idealisation of a  
 154 submesoscale mixed layer front where the bottom of the mixed layer is replaced with a  
 155 flat, rigid boundary. Specifically, an incompressible flow in thermal wind balance with  
 156 uniform horizontal and vertical buoyancy gradients is bounded between two rigid, stress-  
 157 free horizontal surfaces.

158 Non-dimensionalising the Eady problem such that the thermal wind shear,  $M^2/f$ , is  
 159 unity in units where the vertical domain size,  $H = 1$ , brings out four dimensionless  
 160 parameters:

$$\Gamma \equiv \frac{M^2}{f^2}; \quad Re \equiv \frac{H^2 M^2}{f\nu}; \quad Ri \equiv \frac{N^2 f^2}{M^4}; \quad Pr \equiv \frac{\nu}{\kappa}. \quad (2.1)$$

161 Here  $\nu$  is the kinematic viscosity and  $\kappa$  is the diffusivity of buoyancy, but we take  $Pr = 1$ .

162 It should be noted that the Rossby number is not a parameter in this local frontal zone  
163 configuration because there is no horizontal length-scale.

164 We consider a range of front strengths,  $\Gamma = M^2/f^2 \approx [1, 100]$ , which covers a wide  
165 variety of ocean fronts. Although very strong fronts with  $\Gamma > 100$  have been observed  
166 (e.g. Sarkar *et al.* 2016), these fronts are typically very narrow and hence our assumption  
167 of a uniform horizontal density gradient is expected to break down. The development of  
168 SI at very strong ( $\Gamma > 100$ ) and narrow fronts will be reserved for future work.

### 169 2.1. Governing equations

Here, we invoke the Boussinesq approximation with a linear equation of state. We further assume that the Coriolis parameter,  $f$ , is constant and neglect the non-traditional Coriolis terms (i.e. those proportional to  $\hat{f} = 2\Omega \cos \phi$ , where  $\Omega$  is the angular velocity and  $\phi$  is latitude). This ‘traditional’ approximation is made here for simplicity but is shown in appendix A to not qualitatively change our conclusions. The resulting non-dimensionalised Boussinesq equations are

$$\frac{D\mathbf{u}^*}{Dt^*} = -\nabla^* \Pi^* - \frac{1}{\Gamma} \hat{\mathbf{z}} \times \mathbf{u}^* + \frac{1}{Re} \nabla^{*2} \mathbf{u}^* + b^* \hat{\mathbf{z}} \quad (2.2a)$$

$$\frac{Db^*}{Dt^*} = \frac{1}{Re} \nabla^{*2} b^* \quad (2.2b)$$

$$0 = \nabla^* \cdot \mathbf{u}^*. \quad (2.2c)$$

170 Consistent with the non-dimensional parameters (2.1) introduced above, the dimension-  
171 less (\*) variables here are

$$\mathbf{u}^* \equiv \mathbf{u} \frac{f}{HM^2}; \quad b^* \equiv b \frac{f^2}{HM^4}; \quad t^* \equiv t \frac{M^2}{f}; \quad \mathbf{x}^* \equiv \mathbf{x} \frac{1}{H}; \quad \nabla^* \equiv H \nabla. \quad (2.3)$$

172 The dimensionless pressure head acceleration,  $\nabla^* \Pi^*$ , absorbs the hydrostatic pressure  
173 gradient, and is eliminated when writing (2.2a) with the along-front streamfunction.

We choose  $\hat{\mathbf{x}}$  to be the across-front direction (parallel to  $\nabla_h \bar{b}$ ). The background basic state (denoted by an overbar) used for linearisation and the initial condition for the numerical simulations is

$$\begin{aligned} \bar{v}^* &= z^* - 1/2 \\ \bar{b}^* &= \Gamma^{-1} x^* + Ri z^* \end{aligned} \quad (2.4)$$

174 as shown in the grey shaded region of figure 1. Following the Eady model, we will also use  
175 solid horizontal boundaries at  $z^* = 0$  and 1 which are taken to be insulating and stress-  
176 free (Eady 1949). In what follows we will omit the appended asterisks for notational  
177 simplicity. All variables are dimensionless unless the units are explicitly stated (as in  
178 some figures).

### 179 2.2. Primary instability

We begin by linearising the Boussinesq equations (2.2) about the basic state (2.4) to describe the evolution of small anomalies in buoyancy and momentum, denoted with a prime. Since the most unstable mode of SI is independent of the along-front ( $\hat{\mathbf{y}}$ ) direction

(Stone 1966), we consider linear perturbations that vary only in  $x$  and  $z$ :

$$\begin{aligned}
 \partial_t u' &= -\partial_x \Pi' + \frac{1}{\Gamma} v' + \frac{1}{Re} \nabla^2 u' \\
 \partial_t v' + w' \partial_z \bar{v} &= -\frac{1}{\Gamma} u' + \frac{1}{Re} \nabla^2 v' \\
 \partial_t w' &= -\partial_z \Pi' + \frac{1}{Re} \nabla^2 w' + b' \\
 \partial_t b' + u' \partial_x \bar{b} + w' \partial_z \bar{b} &= \frac{1}{Re} \nabla^2 b' \\
 0 &= \nabla \cdot \mathbf{u}'.
 \end{aligned} \tag{2.5}$$

180 We transform this set of PDEs into a set of ODEs by further assuming normal mode  
 181 perturbations autonomous in  $x$  (with wavenumber  $k_x$ ) and in time (with frequency  $\omega$ )  
 182 of the form

$$\chi'(x, z, t) = \Re \left[ \hat{\chi}(z) e^{i(k_x x - \omega t)} \right] \tag{2.6}$$

183 where the eigenfunction,  $\hat{\chi}(z)$ , must then be chosen to satisfy the relevant boundary  
 184 conditions. The set (2.5), after substitution and simplification using the streamfunction  
 185 defined by  $(u', w') = \nabla \times \psi \hat{\mathbf{y}}$ , becomes

$$\left( i\omega + \frac{1}{Re} (-k_x^2 + D^2) \right)^2 (-k_x^2 + D^2) \hat{\psi} = \left( -\frac{1}{\Gamma^2} D^2 - \frac{2ik_x}{\Gamma} D + k_x^2 Ri \right) \hat{\psi}, \tag{2.7}$$

where  $D \equiv d/dz$  for notational ease. Note that this equation is closely related to eq.  
 (14) in Grisouard & Thomas (2016) who formulated the equation in terms of pressure  
 and neglected horizontal diffusion. The boundary conditions for  $\hat{\psi}$  at  $z = 0, 1$  on this 6<sup>th</sup>  
 order ODE are

$$\begin{aligned}
 \hat{\psi} &= 0 \\
 D^2 \hat{\psi} &= 0.
 \end{aligned} \tag{2.8}$$

186 To make this system tractable, we follow the method of Weber (1980) and approximate  
 187 equation (2.7) as a 2<sup>nd</sup> order ODE by writing the vertical diffusion terms as spatially-  
 188 invariant wave modes,

$$\frac{1}{Re} D^2 \hat{\psi} \approx -\frac{1}{Re} k_z^2 \hat{\psi} \tag{2.9}$$

189 with vertical wavenumber  $k_z$ . By neglecting the vertical variations in  $k_z$ , this approxi-  
 190 mation constrains the SI mode angle to be uniform in  $z$ . This is a good approximation  
 191 for large  $Re$  and  $k_z$ , when the effects of diffusion are dominated by the interior of the  
 192 domain. This does consequently prohibit the boundaries from generating vorticity, but  
 193 it is found to not influence the selection or stability of SI, which is only energised by the  
 194 bulk background buoyancy and shear. Equation (2.7) then becomes

$$\left[ \left( i\omega - \frac{k_x^2 + k_z^2}{Re} \right)^2 + \frac{1}{\Gamma^2} \right] D^2 \hat{\psi} + \frac{2ik_x}{\Gamma} D \hat{\psi} - k_x^2 \left[ \left( i\omega - \frac{k_x^2 + k_z^2}{Re} \right)^2 + Ri \right] \hat{\psi} = 0, \tag{2.10}$$

195 which has eigensolutions of the form

$$\hat{\psi} = \exp(i\lambda_1 z) - \exp(i\lambda_2 z) \tag{2.11}$$

196 that match the boundaries if  $\lambda_1 - \lambda_2 = 2\pi n$ , for the chosen eigenmode number,  $n$ .  
 197 Equation (2.10) is thus reduced to a quadratic eigenproblem which may be solved by

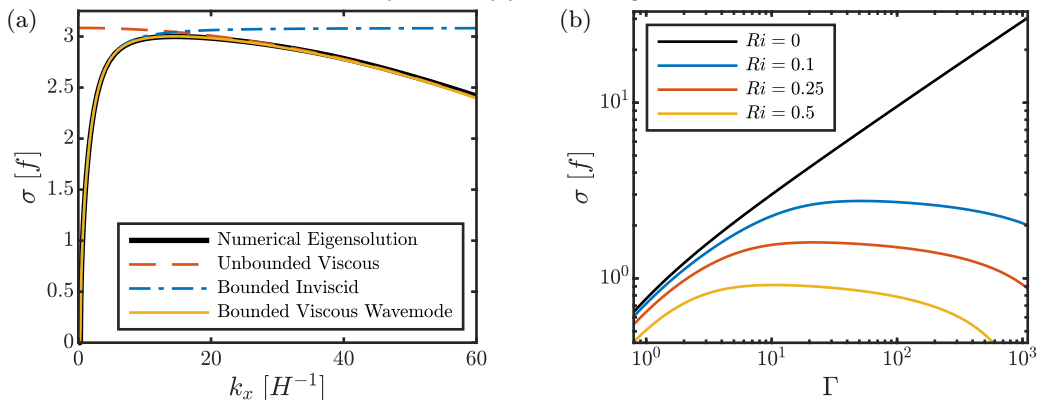


FIGURE 2. (a) The growth rate for the  $n = 1$  SI mode in a vertical front with  $\Gamma = 10$  and  $Re = 10^5$ . The real part of  $\omega$  for the SI modes are everywhere 0 except where linearly stable at very small wavenumber. (b) The growth rate of the fastest growing SI mode ( $n = 1$ ) and wavenumber at  $Re = 10^5$ , as a function of  $\Gamma$ . The vertical front ( $Ri = 0$ ) is shown in black and also for increasing stratification.

198 numerical iteration while enforcing the vertical viscous wave-mode approximation that

$$k_z^2 = \frac{1}{2} (\lambda_1^2 + \lambda_2^2). \quad (2.12)$$

199 Complete details of this solution are included in appendix B.1.

200 The exact numerical eigensolution to the linear set (2.5) was also computed using a  
 201 pseudo-spectral eigenvalue solver written in `Matlab`. The computed solutions to (2.10)  
 202 give good agreement with this numerical solution, as shown in figure 2a, where the  
 203 growth rate,  $\sigma$ , is the imaginary part of  $\omega$ . This new solution correctly accounts for both  
 204 the limiting effects of the vertical boundaries at low wavenumber, and of viscosity at  
 205 high wavenumber. Accurate in the low wavenumber limit, Stone (1971) determined this  
 206 inviscid, bounded solution, where the mode growth becomes suppressed as it feels the  
 207 constraint of the boundaries for  $k_x \lesssim 2\pi$ . In the other limit of unbounded, viscous, and  
 208 hydrostatic motions, Taylor & Ferrari (2009) (and later Bachman & Taylor (2014) for  
 209 non-hydrostatic motions) found that the most unstable mode has a vanishing wavenum-  
 210 ber. The structure of the exact ( $n = 1$ ) viscous, bounded SI mode ( $u'$ ) is shown in the  
 211 background of figure 4. Due to viscous and non-hydrostatic effects, the modes are no  
 212 longer parallel to isopycnals as they were in e.g. Stone (1966).

213 We can now consider how the fastest growing mode of (2.10) varies with  $\Gamma$  and  $Ri$ ,  
 214 as shown in figure 2b. For  $Ri = 0$  the energy growth rate relative to  $f$  increases nearly  
 215 linearly with front strength. However, for strong fronts stratification significantly reduces  
 216 the growth rate of the most unstable modes.

217 In a vertically-unbounded domain with inviscid, hydrostatic dynamics, the  
 218 maximum release of energy can be achieved by motion aligned with  $b$  surfaces, with  
 219  $\theta_b = \tan^{-1}(M^2/N^2)$  from the horizontal (i.e.  $k_x/k_z = M^2/N^2$ ) (Taylor & Ferrari 2009),  
 220 effectively precluding any buoyancy flux. However, in a vertically-bounded front with  
 221 weak stratification, the most unstable modes become very inclined to the isopycnals as  
 222 shown in figure 3a, and reach nearly  $45^\circ$  for  $N^2 = 0$ . While the angle of the unstable SI  
 223 modes must still be between the angle of the isopycnals and surfaces of constant absolute  
 224 momentum ( $\tilde{m} = \tilde{v}_g + \Gamma^{-1}x$ ) (dotted and dash-dotted curves in figure 3a), the most  
 225 unstable modes approach more closely to the angle of the absolute momentum surfaces  
 226 ( $\theta_m = \tan^{-1} \Gamma^{-1}$ ) for small front strength. This permits a larger buoyancy production

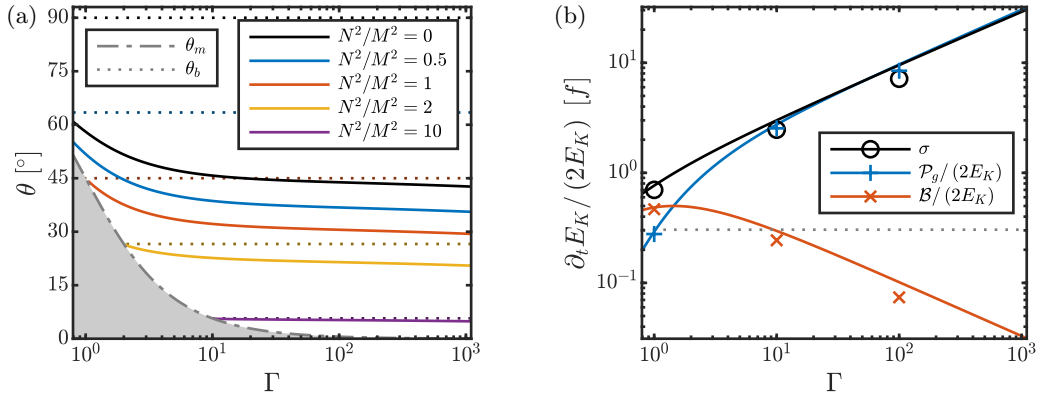


FIGURE 3. (a) The angle of the fastest growing SI mode as measured from horizontal, plotted as a function of front strength,  $\Gamma$ , and for different background stratifications measured by the inverse isopycnal slope,  $N^2/M^2$ . The shaded grey region indicates where  $f q > 0$  and the front is stable to SI. The unstable SI mode inclination must remain between the angle of absolute momentum surfaces ( $\theta_m$ , dot-dashed line) and isopycnals ( $\theta_b$ , dotted lines), which for  $N^2/M^2 = 0$ ,  $\theta_b = 90^\circ$ . This unstratified case has modes nearly equally spaced between the isopycnals and absolute momentum surfaces for large  $\Gamma$ , but with increasingly horizontal isopycnals the SI modes grow more along these isopycnals. While the angle of the contour  $\psi(x, z) = 0$  is a weak function of  $z$  in the full numerical eigenresolution (decreasing by at most 5% at the boundaries), the mode angle of the solutions (2.11) are independent of  $z$ . (See appendix B.1 for details on the calculation of  $\theta$  and the eigenfunctions.) (b) Contribution of the most unstable linear SI mode to the energy budget (4.1) of the vertical front for  $Re = 10^5$ . Normalised by the kinetic energy, the geostrophic shear production and buoyancy flux are related to the growth rate,  $\sigma$ . As expected with SI, the instability still primarily draws energy from the thermal wind shear into the kinetic energy of the mode through the TKE production term. The grey dotted line indicates the growth rate of baroclinic instability for this choice of parameters (Stone 1966). Symbols correspond to the numerical simulations discussed in §3, computed as a time-average from  $t = 0$  to  $\tau_c/2$ .

227 of energy ( $\mathcal{B} = \langle w'b' \rangle$ ), as shown in figure 3b, while the geostrophic shear production  
 228 ( $\mathcal{P}_g = -\langle \bar{v}'w' \partial_z \bar{v}_g \rangle$ ) is the dominant energy source in the rest of the parameter space.  
 229 Here and throughout the rest of this paper,  $\langle \cdot \rangle$  indicates a volume average over the  
 230 entire domain, and primes represent local departures from the horizontally-averaged  
 231 fields denoted by  $\bar{\cdot}$ .

### 2.3. Secondary instability

233 Secondary instability plays a key role in the equilibration of SI. Here, we explore  
 234 the onset of secondary instability to determine the cumulative effects of SI in the front  
 235 equilibration energetics and the contribution to mixing down the thermal wind shear.

236 As described in Taylor & Ferrari (2009), shear associated with the growing SI modes  
 237 becomes unstable to a secondary Kelvin–Helmholtz instability (KHI) which prompts a  
 238 transition to turbulence. We identify this critical SI mode amplitude,  $U_{SI} = U_c$ , at which  
 239 the SI modes themselves break down as the time when the SI growth rate,  $\sigma_{SI}$ , is equal  
 240 to the Kelvin–Helmholtz instability growth rate,  $\sigma_{KH}$ . Of course,  $\sigma_{KH}$  is a monotonically  
 241 increasing function of the shear, and thereby of  $U_{SI}$  which exponentially grows at a rate  
 242  $\sigma_{SI}$ . We therefore iteratively compute the secondary linear stability of the combined Eady  
 243 and growing SI mode basic state to determine this critical amplitude that is plotted in  
 244 figure 5a.

245 We formulate the 1D linear Kelvin–Helmholtz stability problem using a sinusoidal  
 246 extension of the structure of the full SI mode (evaluated at the mid-plane) in the rotated  
 247 coordinates shown in figure 4. As described in appendix C, this basic state includes the

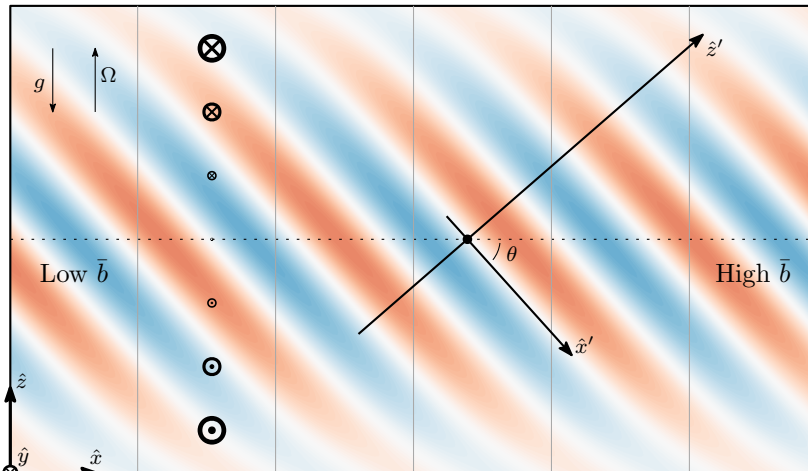


FIGURE 4. Diagram showing the secondary stability analysis coordinate transformation drawn over the linear SI mode ( $u'$ ). The primary SI basic state is also indicated, with grey isopycnal lines showing the linearly increasing buoyancy from left to right (for  $Ri = 0$ ), as well as the thermal wind vectors into the page which balance the baroclinic torques.

248 constant vertical and horizontal buoyancy gradients associated with the basic state in  
 249 the Eady model as well as the buoyancy changes induced by the SI modes. We iteratively  
 250 compute  $\sigma_{\text{KH,max}}(U_{\text{SI}})$  with a pseudo-spectral solver until finding the critical SI mode  
 251 amplitude,  $U_c$ . While the most unstable SI wavevector,  $|\mathbf{k}_{\text{SI}}|$ , increases as the mode  
 252 number ( $n$ ) and  $Re$  increase, the scaling for  $U_c$  appears to be dominated by  $\sigma_{\text{SI}}$  and so  
 253 remains largely unchanged.

254 We demonstrate this here just for the unstratified ( $Ri = 0$ ) front, but a general analysis  
 255 is provided in appendix C. Figure 5a shows the classic KH stability analysis (i.e. ignoring  
 256 rotation and neglecting the along-mode component of the background stratification)  
 257 alongside the full solution for  $U_c$ . The dashed line shows the resulting scaling,

$$U_c \propto \left( \sqrt{\Gamma} |\mathbf{k}_{\text{SI}}| \right)^{-1} \quad (2.13)$$

258 (in our same dimensionless units of the velocity associated with thermal wind shear).  
 259 We obtain this scaling by balancing the KHI growth rate (proportional to the non-  
 260 dimensional shear in the SI mode,  $\sigma_{\text{KH}} \propto U_c |\mathbf{k}_{\text{SI}}|$ ) with the SI growth rate in the limit of  
 261 large  $\Gamma$ ,  $\sigma_{\text{SI}} \propto \Gamma^{-1/2}$ . We see that this simple scaling argument fails for small  $\Gamma$  where  
 262 the growth rate in these weak fronts is slow compared to  $f$ .

### 263 3. Numerical simulations

264 We employed the non-hydrostatic hydrodynamics code, DIABLO, to verify the conclu-  
 265 sions of the preceding linear primary and secondary instability theory as well as the results  
 266 in the following two sections. DIABLO solves the fully nonlinear Boussinesq equations  
 267 (2.2) on an  $f$ -plane (Taylor 2008). Second-order finite differences in the vertical and a  
 268 collocated pseudo-spectral method in the horizontal periodic directions are employed,  
 269 along with a third-order accurate implicit-explicit time-stepping algorithm using Crank-  
 270 Nicolson and Runge-Kutta with an adaptive step size. Rigid, stress-free, and insulating  
 271 horizontal boundaries are enforced to match the linear analysis in §2. Following Taylor  
 272 & Ferrari (2009), the simulations are run in a 2D ( $x$ - $z$ ) domain while retaining all three

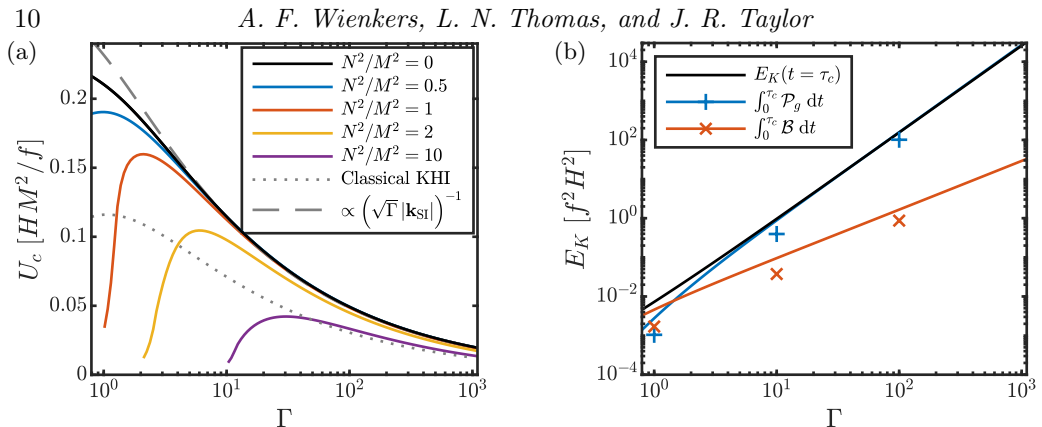


FIGURE 5. (a) The critical amplitude of the most unstable SI mode velocity at which secondary instability begins to dominate, shown in units of the thermal wind. The dotted line shows this critical amplitude when rotation and along-shear stratification (i.e.  $x^\dagger$  in appendix C) are neglected in the KHI stability analysis. The dashed line shows the scaling (2.13) achieved by taking the KHI growth rate directly proportional to the shear and matching  $U_c$  in the limit of large  $\Gamma$ . (b) The cumulative KE budget contributions from the  $n = 1$  linear SI mode of the unstratified front, integrated through  $U_c$ . Coloured symbols show the value derived from the 2D simulations. Due to weak scale and mode selection, these simulations contain a range of  $n$  and  $k_x$ , yet with increasing front strength the values calculated from the simulations approach the  $n = 1$  line shown due to stronger mode selection as the higher modes are damped by viscosity.

273 components of the velocity vector. This choice allows us to focus on the evolution and  
274 saturation of the symmetric modes.

275 While the presented analytical results in this paper are general, we focus these numeri-  
276 cal verification experiments on an initially unstratified front ( $Ri = 0$ ) with  $Re = 10^5$ .  
277 It should be noted that the along-front flow would be susceptible to KHI in a three-  
278 dimensional simulation, but this is not considered for the purpose of this study. Each of  
279 the simulations were initialised as a balanced front (2.4) with strength  $\Gamma = \{1, 10, 100\}$   
280 and white noise was added to the velocity with a (dimensionless) amplitude of  $10^{-4}$ . The  
281 simulations were run through the linear phase until secondary instability breaks down the  
282 SI modes at the critical time,  $\tau_c$ , as shown in the right column of figure 6. At this point,  
283 we measure the cumulative effects of SI on the front — the integrated shear production,  
284 buoyancy fluxes, and momentum transport — and present these values alongside the  
285 analytical results of §4 and §5. While we restrict these verification simulations to initially  
286 unstratified fronts and do not consider times after  $\tau_c$ , we extend these simulations in a  
287 companion paper to explore the SI-induced re-stratification and geostrophic adjustment  
288 of the fronts at later times.

#### 289 4. Energetics of SI

290 In light of these stability analyses, a natural question is: What impact does the linear  
291 SI phase and ensuing turbulence have on the resulting equilibration of the front, and how  
292 does it depend on the frontal strength? To answer this, we combine the primary linear  
293 instability results of §2.2 with the details of SI saturation from §2.3 to determine the  
294 cumulative contribution of SI modes up to the critical time,  $\tau_c = \sigma_{SI}^{-1} \log(U_c/U_0)$ , when  
295 SI has grown to an amplitude  $U_c$ . This allows us to quantify the energetics of the linear  
296 SI modes and their influence on the evolution of the front.

297 With the complex eigenfunction,  $\hat{\psi}$ , found by iteratively solving for  $\lambda_1$  and  $\lambda_2$  in  
298 equation (2.11), we determined the full structure of these modes:  $\hat{u}$ ,  $\hat{v}$ ,  $\hat{w}$ , and  $\hat{b}$  as

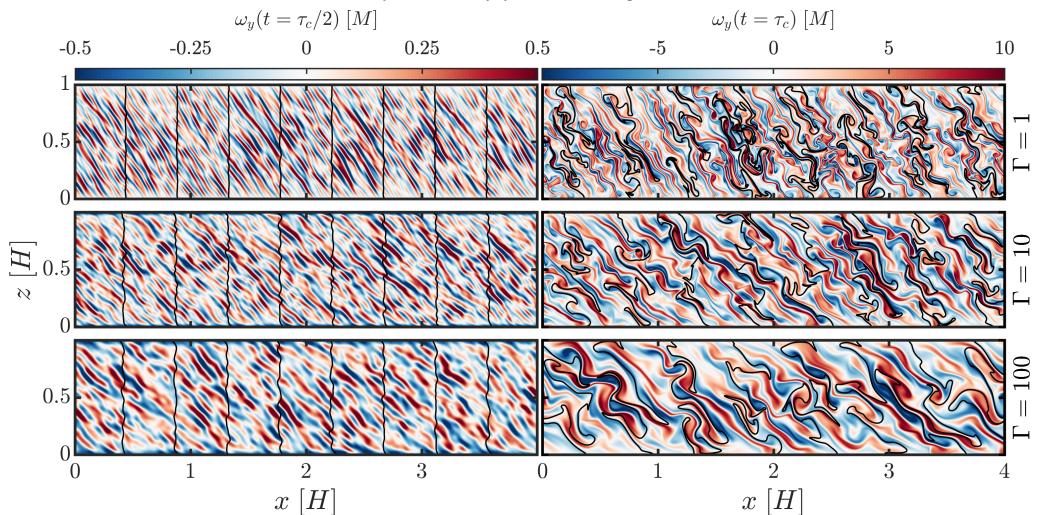


FIGURE 6. Slices across each front show the along-front vorticity,  $\omega_y$ , along with buoyancy contours (black lines), for  $\Gamma = 1$  (top), 10 (centre), and 100 (bottom). Two snapshots are shown, at  $t = \tau_c/2$  (left) when the fastest linear SI mode has emerged, and at  $t = \tau_c$  (right) when secondary KHI first begins to break the coherent energy of the SI modes into small-scale turbulence. Note that the vorticity is normalised by  $M$ , which keeps the amplitude similar across the range of  $\Gamma$  (consistent with the scaling (2.13)). The vorticity normalised by  $f$  can be obtained by multiplying the values shown here by  $\Gamma^{-1/2}$ . During the linear growth phase (left panels), the SI modes do not align with the isopycnals, and rather become increasingly flat for larger  $\Gamma$ , consistent with the results shown in figure 3a).

300 given in appendix B.1. With these, we compute the correlations relevant to the transport  
 301 and energetics of the development of SI. We first must normalise each of the modes by  
 302  $\sqrt{|\hat{u}|^2 + |\hat{w}|^2}$ , and then rewrite them in the normal mode form, (2.6), using the parameter  
 303 and eigenvalues of equation (2.10).

304 We will first consider the contribution of SI to the turbulent kinetic energy (TKE),  
 $E_K \equiv \frac{1}{2} \langle u'_i u'_i \rangle$ :

$$\frac{\partial E_K}{\partial t} = - \underbrace{\langle \overline{u'w'} \frac{\partial \bar{u}}{\partial z} \rangle}_{-\mathcal{P}_x} - \underbrace{\langle \overline{v'w'} \left( \frac{\partial \bar{v}_a}{\partial z} + \frac{\partial \bar{v}_g}{\partial z} \right) \rangle}_{-\mathcal{P}_y} + \underbrace{\langle w'b' \rangle}_{\mathcal{B}} - \underbrace{\frac{1}{Re} \langle \frac{\partial u'_i}{\partial x_j} \frac{\partial u'_i}{\partial x_j} \rangle}_{\varepsilon_t}. \quad (4.1)$$

305 The first two terms on the RHS represent the shear production,  $\mathcal{P}$ , converting energy  
 306 from the mean flow into TKE. Specifically, the along-front contribution ( $\mathcal{P}_y$ ) is split into  
 307 a geostrophic shear production term,  $\mathcal{P}_g$ , energised by the thermal wind shear, and an  
 308 ageostrophic part. The other potential source of TKE comes from buoyancy production,  
 309  $\mathcal{B}$ , which represents the transfer of energy from PE into TKE. The cumulative generation  
 310 of TKE by each of these terms in (4.1), integrated from  $t = 0$  up to transition at  $\tau_c$  is  
 311 shown in figure 5b. As expected for SI, the contribution from  $\mathcal{P}_g$  exceeds  $\mathcal{B}$ , except  
 312 for small  $\Gamma$ . Interestingly, even for these SI modes that are very flat (i.e. inclined to  
 313 the isopycnals) in strong fronts, the energetics are still dominated by geostrophic shear  
 314 production which relies on the vertical velocity to exchange geostrophic momentum.  
 315 We confirm this result using the numerical simulations described in §3. Even though  
 316 the initial white noise and weak mode selection mean that a range of wavenumbers are  
 317 represented in the simulations, these predictions still remain robust.

318 Following Haine & Marshall (1998), it is possible to re-frame the SI stability criterion,

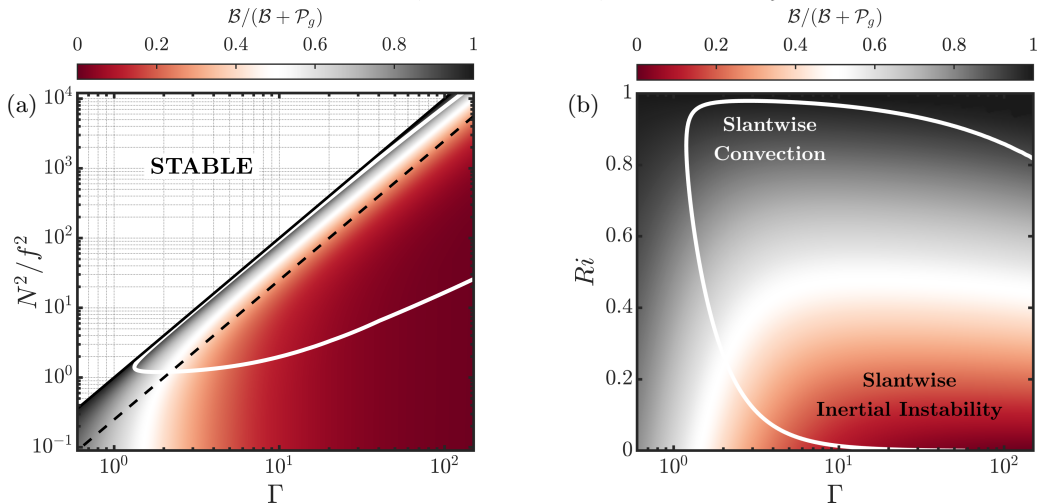


FIGURE 7. Contours of the production ratio (4.4) distinguish regions where geostrophic shear production dominates (0) and regions that buoyancy production dominates (1). The white line separates regions of parameter space where SI modes are more aligned with isopycnals, i.e.  $|\theta - \theta_b| < |\theta - \theta_m|$  (inside), from the regions (outside) where they are more closely aligned with absolute momentum surfaces. (a) The production ratio plotted in parameter space with  $N^2/f^2$  on the  $y$ -axis, chosen so that the axes are only interdependent on  $f$ . A black dashed line designates the contour  $Ri = 0.25$ . Lines of constant isopycnal slope ( $M^2/N^2$ ) are straight lines of slope 1 in this log-log scale. Strong fronts with weak stratification (equivalently, large isopycnal slope) derive energy primarily from geostrophic shear production. Thus, rapid frontogenesis (moving horizontally to the right), or rapid de-stratification via mixing (moving vertically downwards) will tend the SI modes to slantwise inertial instability. (b) The parameter space is rescaled with  $Ri$  on the  $y$ -axis to emphasise the region near  $Ri = 1$  where SI in a balanced front becomes stabilised. Non-hydrostatic effects (for small  $\Gamma$ ) and boundary viscous effects (for large  $Ri$ ) influence the SI modes to derive this portion of energy from the background buoyancy gradient. Non-traditional effects also influence how SI extracts energy, as shown by figure 10 in appendix A.2.

319  $f q < 0$ , in terms of the energy sources driving growth: the background buoyancy gradient  
 320 and the geostrophic kinetic energy. First consider fluid parcels that are constrained to  
 321 move along isopycnals (and thus incur no gravitational penalty). The criterion,  $f q < 0$ ,  
 322 for instability then becomes the Rayleigh criterion describing inertial instability,

$$f \left( \frac{\partial m}{\partial x} \right)_b < 0. \quad (4.2)$$

323 Since they are aligned with the isopycnals, these modes do not extract potential energy  
 324 from the front and instead grow by drawing energy from the thermal wind. Contrast  
 325 this with the other limiting angle that SI modes can take, when their motion is aligned  
 326 with surfaces of constant absolute momentum. Now, instability requires that the vertical  
 327 buoyancy gradient measured along these absolute momentum surfaces is negative:

$$\left( \frac{\partial b}{\partial z} \right)_m < 0. \quad (4.3)$$

328 Therefore, motions that are constrained to follow absolute momentum surfaces can  
 329 extract potential energy, analogously to ‘upright convection’ (Haine & Marshall 1998).  
 330 For hydrostatic perturbations in an unbounded domain, the most unstable mode of SI is  
 331 aligned with the isopycnals and hence grows by extracting kinetic energy from the thermal

332 wind through geostrophic shear production (Stone 1972; Haine & Marshall 1998; Taylor  
333 & Ferrari 2009).

334 As shown previously in figure 3a, for non-hydrostatic modes in a bounded domain, the  
335 most unstable mode of SI is not necessarily aligned with isopycnals and hence these modes  
336 can grow through a non-trivial combination of buoyancy production and geostrophic  
337 shear production. We can quantify the energetic influences on the most unstable mode of  
338 SI using the linear stability analysis up to the critical time,  $\tau_c$ . We do this by introducing  
339 the energy production ratio,

$$\frac{\mathcal{B}}{\mathcal{B} + \mathcal{P}_g} = \frac{\lambda_1 + \lambda_2}{2k_x\Gamma}, \quad (4.4)$$

340 as plotted in figure 7, where  $\mathcal{B}$  is the buoyancy flux,  $\mathcal{P}_g$  is the geostrophic shear  
341 production, and  $\lambda_1$  &  $\lambda_2$  describe the vertical mode structure (2.11) and depend on  $Ri$  and  
342  $\Gamma$  (details which are given in appendix B.2). The production ratio suggests the expected  
343 character of SI. For strong fronts with weak vertical stratification, SI extracts energy from  
344 shear production, and so we refer to this flavour of SI as ‘slantwise inertial instability.’ In  
345 the inviscid and hydrostatic limits, the linear analysis indicates that energy is always fully  
346 derived from geostrophic shear production, with modes aligned perfectly with isopycnals  
347 at  $\theta_b$ . Non-hydrostatic effects flatten the SI modes particularly for small  $\Gamma$ . This permits  
348 buoyancy production to contribute to the energy more than shear production, and so  
349 we call this flavour of SI ‘slantwise convection.’ Note that this term has sometimes been  
350 used synonymously with SI in the literature, although it is not always congruous with  
351 the energetics of SI (Haine & Marshall 1998). The boundary-permitted viscous limit in  
352 figure 7b each for large  $\Gamma$  and large  $Ri$  also exhibits slantwise convection modes. It is  
353 perhaps then surprising that within the white outlined region, indicating where SI modes  
354 are more aligned with isopycnals, the instability does not always extract a majority of  
355 energy from the shear production (i.e. red shading).

356 In the ‘slantwise convection’ regime, where  $\mathcal{B} > \mathcal{P}_g$ , SI tends to be weak and the  
357 total energy production is small. This raises the question of whether it is important to  
358 account for the SI-driven buoyancy flux in parameterisations of SI. To provide context, we  
359 compare the SI-driven buoyancy flux at  $\tau_c$  to the buoyancy flux associated with mixed  
360 layer instability (MLI) in the parameterisation from Fox-Kemper *et al.* (2008). They  
361 empirically estimated a constant efficiency factor for the finite-amplitude MLI, which in  
362 our nondimensional variables can be written

$$C_e = \Gamma^{-1} \langle \overline{w'b'} \rangle_{\text{MLI}} = 0.06 - 0.08. \quad (4.5)$$

363 In comparison a typical SI buoyancy flux at  $\tau_c$  for the slantwise convective regime  
364 (specifically at  $\Gamma = 1$  and  $Ri = 0$ ) is

$$\Gamma^{-1} \langle \overline{w'b'} \rangle_{\text{SI},c} = 0.0074. \quad (4.6)$$

365 Note that the buoyancy flux increases in time during the growing phase of SI and MLI.  
366 The fact that  $\langle \overline{w'b'} \rangle_{\text{SI}}$  at  $t = \tau_c$  is smaller than  $\langle \overline{w'b'} \rangle_{\text{MLI}}$  highlights the comparatively  
367 early saturation of SI through secondary instabilities. Thus even though MLI grows more  
368 slowly for this set of parameters (cf. the dotted line in figure 3b), the finite-amplitude  
369 buoyancy flux associated with MLI has a significantly larger influence on the rate of  
370 re-stratification compared to SI for weak fronts ( $\Gamma = 1$ ). For stronger fronts with weak  
371 vertical stratification (i.e. large  $\Gamma$  and small  $Ri$ ) where the geostrophic shear production is  
372 larger than the buoyancy flux, SI can indirectly induce re-stratification by first generating  
373 large vertical fluxes of geostrophic momentum. This will be discussed in the next section.

## 5. Momentum transport by SI

We now consider the effect that SI has on the geostrophic shear and the implications for the subsequent response of the front.

### 5.1. Dominant momentum balance

We would like to determine the dominant terms in the mean horizontal momentum equations to understand what is driving the evolution of the front. Subtracting off the background geostrophic velocity and buoyancy gradient from the Boussinesq equation (2.2a) gives a horizontally-autonomous system allowing us to Reynolds average in the  $\hat{\mathbf{x}}$  and  $\hat{\mathbf{y}}$  directions. Using continuity and geostrophic balance, the horizontal ageostrophic momentum equations are

$$\partial_t \bar{u}_a + \partial_z \overline{u'w'} = \Gamma^{-1} \bar{v}_a \quad (5.1a)$$

$$\partial_t \bar{v}_a + \partial_z \overline{v'w'} = -\Gamma^{-1} \bar{u}_a. \quad (5.1b)$$

To determine the dominant balance at early times arising from the growing SI modes, we first assume the Coriolis term in equation (5.1b) is small. With this approximation, we construct a ratio from the terms in equation (5.1a),

$$\frac{\partial_z \overline{u'w'}}{\Gamma^{-1} \bar{v}_a} \approx -\frac{\partial_z \overline{u'w'}}{\Gamma^{-1} \int_0^\tau \partial_z \overline{v'w'} dt} = 2\Gamma^2 \sigma^2 \frac{\lambda_1 + \lambda_2}{\lambda_1 + \lambda_2 - 2k_x \Gamma} \quad (5.2)$$

$$\sim 2 \text{ for } \Gamma \gg 1 \text{ and } Ri = 0,$$

where we have also assumed exponential growth in time,  $\propto \exp(\sigma t)$ . We take  $U_{SI}$  at  $t = 0$  to be infinitesimal so that the lower limit of integration evaluates to 0. The arbitrary upper limit,  $\tau$ , then cancels with the exponential evaluated at  $\tau$  in the numerator. Similarly for the terms in the  $y$ -momentum equation (5.1b), the ratio is

$$\frac{\partial_z \overline{v'w'}}{-\Gamma^{-1} \bar{u}_a} \approx \frac{\partial_z \overline{v'w'}}{\Gamma^{-1} \int_0^\tau \partial_z \overline{u'w'} dt} = 2 \frac{\lambda_1 + \lambda_2 - 2k_x \Gamma}{\lambda_1 + \lambda_2} \quad (5.3)$$

$$\sim 2\Gamma \text{ for } \Gamma \gg 1 \text{ and } Ri = 0,$$

where we again use the solution for the eigenfunctions (B7) derived in appendix B.1 to evaluate these integrals. Each of these expressions in (5.1b) are self-consistent with our assumption to neglect the Coriolis term if both ratios are  $\gg 1$ . We found this to be the case for  $\Gamma \gtrsim 1$  &  $Ri \lesssim 0.5$  and so we conclude that the mean ageostrophic  $y$ -momentum is driven more strongly than the  $x$ -momentum — i.e. the dominant balance is initially  $\partial_t \bar{v}_a \approx -\partial_z \overline{v'w'}$ .

### 5.2. Loss of geostrophic balance

This dominant balance with the  $\partial_z \overline{v'w'}$  Reynolds stress term suggests that at first order SI can influence the large-scale evolution of the front by rearranging the momentum of the balanced thermal wind. The rate at which this geostrophic shear profile is reduced will give hints as to the type of adjustment that follows SI.

Taking the vertical gradient of the dominant momentum balance,

$$\frac{\partial}{\partial t} (\partial_z \bar{v}) \approx -\partial_z^2 \overline{v'w'}, \quad (5.4)$$

we can estimate the time-scale required to mix the thermal wind shear:

$$\tau_{\text{mix}} = \frac{\partial_z \bar{v}_g}{\langle \partial_z^2 \overline{v'w'} \rangle_c}, \quad (5.5)$$

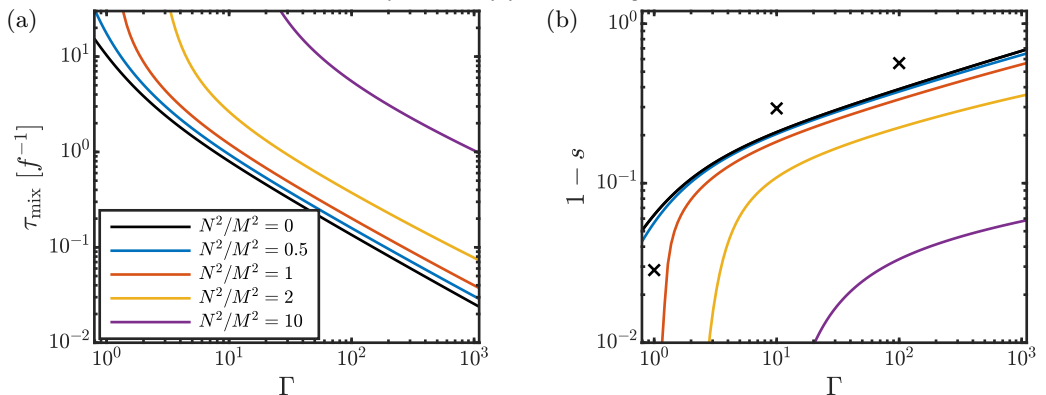


FIGURE 8. (a) The mixing time-scale (5.5) required for SI-driven fluxes to entirely destroy the thermal wind shear. Strong fronts with steep isopycnals are rapidly mixed (relative to an inertial period) whereas this time-scale becomes longer than an inertial period for small  $\Gamma$ . (b) The thermal wind shear mixing fraction,  $(1 - s)$ , induced by SI (5.9). Colours correspond to the different values of inverse isopycnal slope,  $N^2/M^2$ , shown in the legend at left. Symbols show the extracted values from the 2D simulations. Momentum is only rearranged within the domain by the linear modes, and so the domain average is conditioned on positive fluxes.

398 for SI momentum fluxes evaluated at  $\tau_c$ . This value is plotted for each  $\Gamma$  in figure 8a, and  
 399 details of the calculation are saved for appendix B.3. If this time-scale is long compared  
 400 to  $f$  (as for very weak fronts), then we might expect the front to slowly slump over while  
 401 remaining quasi-balanced. In contrast, when the vertical fluxes rapidly (relative to  $f$ )  
 402 mix down the thermal wind shear before inertial effects can influence the large-scale  
 403 dynamics, then the response can be viewed as a form of geostrophic adjustment. This is  
 404 the case for  $\Gamma \gtrsim 10$ .

405 Tandon & Garrett (1994) showed that in the limit of instantaneous mixing (here  
 406 for  $\Gamma \gg 1$ ) this resulting geostrophic adjustment of the front results in inertial shear  
 407 oscillations. They considered the evolution of a mixed layer front when a fraction  $(1 - s)$   
 408 of the vertical shear is removed, such that initially

$$\partial_z \bar{v}|_{t=0} = s \partial_z \bar{v}_g. \quad (5.6)$$

409 The subsequent horizontally-invariant inertial oscillations modulate the background  
 410 stratification by differentially advecting the lateral buoyancy gradient across the front.  
 411 Assuming the PV remains constant, the (dimensionless) stratification evolves according  
 412 to

$$\partial_z \bar{b}_i = (1 - s) (1 - \cos(\Gamma^{-1}t)) + Ri_0. \quad (5.7)$$

These inertial oscillations draw closed circular orbits and have a linear structure in  $z$ :

$$\bar{u}_i = -(1 - s) (z - 1/2) \sin(\Gamma^{-1}t) \quad (5.8a)$$

$$\bar{v}_i = s (z - 1/2) + (1 - s) (z - 1/2) (1 - \cos(\Gamma^{-1}t)). \quad (5.8b)$$

413 The amplitude of these inertial shear oscillations are dimensionally  $(1 - s) M^2/f$ .

### 5.3. Inertial oscillation amplitude

414  
 415 The reduction in thermal wind shear before  $\tau_c$  thus should dictate the amplitude of  
 416 these inertial oscillations in a front following SI. We can estimate this mixing fraction,  
 417  $(1 - s)$ , as introduced in Tandon & Garrett (1994). Again using the vertical derivative of  
 418 the dominant momentum balance (5.4), we compute the cumulative contribution of the

419 SI modes through to  $\tau_c$ :

$$1 - s = \int_0^{\tau_c} \langle \partial_z^2 \overline{v'w'} \rangle dt \quad (5.9)$$

420 (detailed in appendix B.3). Note that the term on the right-hand side has been non-  
 421 dimensionalised by  $M^2/f$  (consistent with the dimensionless units used throughout this  
 422 paper) so that  $(1 - s)$  is interpreted as a fraction of the thermal wind shear. This mixing  
 423 fraction is shown in figure 8b. We see that with increasing front strength the linear SI  
 424 modes are able to remove a larger fraction of the thermal wind shear before  $\tau_c$ , setting  
 425 up larger inertial oscillations. While these results combine the analysis of SI with the  
 426 theory of Tandon & Garrett (1994), in a companion paper we consider the direct and  
 427 indirect nonlinear effects of SI on the evolution of these inertial oscillations.

## 428 6. Conclusions

429 Symmetric instability (SI) occurs at density fronts in the ocean and atmosphere when  
 430 the potential vorticity takes the opposite sign to the Coriolis parameter, i.e.  $f q < 0$ . While  
 431 previous studies have focused on the effect of Richardson number on SI, here we have  
 432 explored the dependence of SI on front strength, parameterised by  $\Gamma = M^2/f^2$ , where  
 433  $M^2$  is the horizontal buoyancy gradient. To that end, we have analysed an idealised  
 434 model of a frontal region initially in thermal wind balance with a uniform horizontal  
 435 buoyancy gradient and a constant background vertical stratification. Although highly  
 436 idealised, this configuration was motivated by rapid mixing events such as the passage  
 437 of a storm or an event which vertically mixes the buoyancy profile.

438 Using a linear stability analysis in a vertically-bounded domain with viscous and non-  
 439 hydrostatic effects, we have shown that SI can grow via two routes: by converting kinetic  
 440 energy associated with the balanced thermal wind into the growing perturbations, or by  
 441 extracting potential energy from the front via the buoyancy flux. For strong fronts and  
 442 where  $Ri \lesssim 0.5$ , the larger contribution energising the instability comes from geostrophic  
 443 shear production, but for large  $Ri$  and/or weak fronts the buoyancy flux is also important.  
 444 We have characterised the two limiting behaviours of symmetric instability distinguished  
 445 by the dominant energy source: ‘slantwise convective instability’ extracts energy from the  
 446 background potential energy via buoyancy production with modes tending along absolute  
 447 momentum surfaces, while ‘slantwise inertial instability’ is energised by shear production  
 448 and has more upright modes nearly along isopycnals.

449 This finding provides context to the work by Grisouard (2018) on mixed ‘Inertial-  
 450 Symmetric Instability.’ By varying the Rossby number, they found that while the two  
 451 limiting instabilities extract energy via shear production, buoyancy fluxes can still be  
 452 important for the mixed modes. Here we have focussed on pure SI ( $\partial_x \bar{v} = 0$ ), and found  
 453 that even in this limit the dominant energy source depends on the details of the front.  
 454 However, for the parameters where the buoyancy flux is the largest energy source (the  
 455 ‘slantwise convection’ regime), the SI-driven buoyancy flux is small compared to the  
 456 mixed layer eddy parameterisation of Fox-Kemper *et al.* (2008). Nonetheless, at stronger  
 457 fronts SI can induce rapid re-stratification by first generating large vertical fluxes of  
 458 geostrophic momentum, as parameterised by Bachman *et al.* (2017).

459 By extracting energy from the balanced thermal wind, SI leads to re-stratification,  
 460 and can induce vertically-sheared inertial oscillations depending on the strength of the  
 461 front. The mixing time-scale for SI to homogenise the thermal wind shear decreases with  
 462 front strength, and is faster than an inertial period for  $\Gamma \gtrsim 10$ . Thus the response to  
 463 rapid mixing of the thermal wind shear at strong fronts can be described in terms of

464 geostrophic adjustment. We analysed this behaviour in the context of the model used  
 465 in Tandon & Garrett (1994) which assumed that the potential vorticity was constant  
 466 throughout the adjustment process. Using the linear stability analysis, we estimated the  
 467 degree to which SI mixes the thermal wind shear and concluded that SI can generate  
 468 large amplitude inertial oscillations at strong fronts.

469 In Part 2 of this series, we consider the nonlinear consequences of these findings well  
 470 beyond the saturation point of SI. We continue the numerical simulations presented here  
 471 to study the long-term evolution of initially unstratified fronts. In particular, we focus  
 472 on the equilibration of the front and how the details depend on the particular flavour of  
 473 SI and the front strength.

## 474 Appendix A. Non-traditional Coriolis effects

### 475 A.1. Non-traditional governing equations

476 In the following appendices we will detail and generalise our bounded, viscous, and non-  
 477 hydrostatic analysis without neglecting the horizontal component of Earth's rotation. The  
 478 influence of these so-called 'non-traditional' terms on SI has been previously explored in  
 479 the inviscid limit by Colin de Verdière (2012) and for unbounded modes by Zeitlin (2018).

480 One consequence of the traditional approximation we used in the analysis thus far is  
 481 that the dynamics are independent of the front orientation. We therefore only specified  
 482 that  $\hat{\mathbf{x}}$  points across the front (parallel to  $\nabla_h \bar{b}$ ). However, the non-traditional terms break  
 483 this horizontal isotropy, and so we must specify the angle,  $\vartheta$ , of the background buoyancy  
 484 gradient relative to north. We still take  $x$  to be across-front (i.e.  $|\nabla_h \bar{b}| = \partial_x \bar{b} = M^2$ ), but  
 485 we now orient the entire front (and  $\hat{\mathbf{x}}$ ) an angle  $\vartheta$  from north.

486 Including the northward horizontal component of Earth's rotation, the Boussinesq  
 487 momentum equation (2.2a) becomes

$$\frac{D\mathbf{u}^*}{Dt^*} = -\nabla^* \Pi^* - \frac{1}{\Gamma} (\gamma \hat{\mathbf{x}} + \alpha \hat{\mathbf{y}} + \hat{\mathbf{z}}) \times \mathbf{u}^* + \frac{1}{Re} \nabla^{*2} \mathbf{u}^* + b^* \hat{\mathbf{z}}. \quad (\text{A } 1)$$

488 The importance of these non-traditional terms is measured by

$$\gamma \equiv \frac{\tilde{f}}{f} \cos \vartheta = \frac{\cos \vartheta}{\tan \phi}, \quad (\text{A } 2)$$

489 which accounts for both the latitude ( $\phi$ ) and the orientation ( $\vartheta$ ) of the across-front  
 490 ( $x$ -axis) relative to north.  $\alpha$  is the 'symmetric' component of  $\tilde{f}$  in the along-front ( $\hat{\mathbf{y}}$ )  
 491 direction, and drops out upon writing (A 1) with the streamfunction. So while the front  
 492 orientation and latitude are both important when considering non-traditional effects,  
 493 these can be reduced into the single parameter  $\gamma$ .

494 It becomes apparent now that the traditional approximation ( $\gamma \rightarrow 0$ ) used to simplify  
 495 the analysis in §2 holds better at mid to high latitudes and for fronts with a nearly  
 496 east/west lateral density gradient. Additionally, the importance of this horizontal com-  
 497 ponent is diminished in the large shear regime of the strong fronts we considered, where  
 498 the vorticity from the thermal wind shear ( $M^2/f$ ) greatly exceeds  $\tilde{f}$  (i.e. when  $\gamma/\Gamma \ll 1$ ).

### 499 A.2. Non-traditional results at $\phi = 45^\circ$

500 To demonstrate the effects of the non-traditional terms on the main results in this  
 501 paper, we present a selection of these results for  $\phi = 45^\circ$ , and for  $\vartheta = 0^\circ$  &  $180^\circ$ . We find  
 502 that while the horizontal component of Earth's rotation quantitatively influences the SI  
 503 growth and transport properties, it does not qualitatively change the observed trends  
 504 and our conclusions.

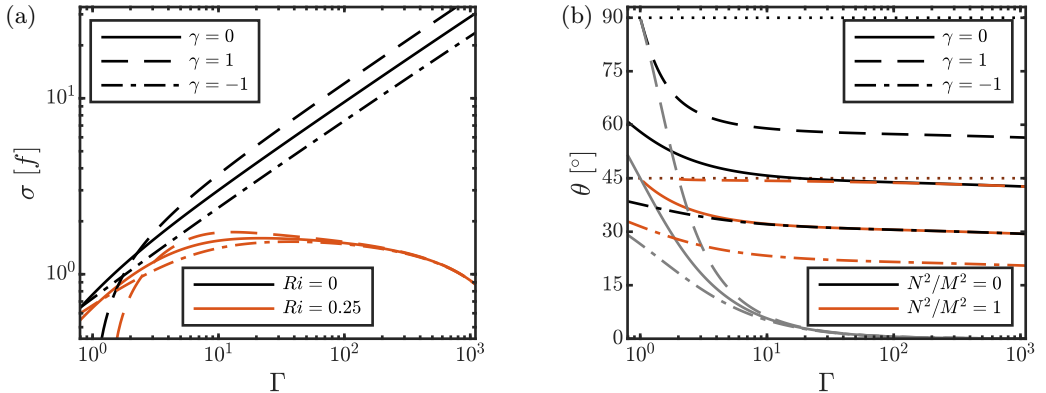


FIGURE 9. (a) The growth rate of the fastest growing SI mode as a function of  $\Gamma$ , for both axisymmetric front orientations at  $\phi = 45^\circ$  and compared to the traditional approximation ( $\gamma = 0$ ) as in figure 2b. Stratification suppresses the non-traditional effects, and so the lines for  $Ri = 0.25$  collapse at larger values of  $\Gamma$ . (b) The angle of the fastest growing SI mode as measured from horizontal, plotted as a function of  $\Gamma$  for the same two front orientations at latitude  $\phi = 45^\circ$  and the traditional approximation ( $\gamma = 0$ ) matching figure 3a. The two isopycnal slope angles are indicated with dotted lines, and the angle of absolute momentum surfaces ( $\theta_m$ ) are shown in grey.

505 The non-traditional terms impact the stability of SI by changing the contours of  
 506 absolute momentum,

$$\bar{m} = \bar{v}_g + \frac{1}{\Gamma}x - \frac{\gamma}{\Gamma}z. \quad (\text{A } 3)$$

507 (Recall  $x$  is still the across-front coordinate, but now the entire front has been oriented  
 508  $\vartheta$  from north.) This means that for the range  $\Gamma < \gamma$ , the front is stable to SI. This  
 509 is written equivalently as a sub-critical Richardson number,  $Ri_c = 1 - \gamma/\Gamma$ . Of course  
 510 it should be emphasised that at  $\phi = 45^\circ$ ,  $\gamma = 1$  only if the high buoyancy side is  
 511 further north ( $\vartheta = 0^\circ$ ). In the opposite orientation (when the buoyancy gradient points  
 512 south) then  $\gamma = -1$ . Thus non-traditional effects can either increase or decrease the  
 513 region of instability (in  $Ri$ - $\Gamma$  space) and consequently influences the growth rate. This is  
 514 apparent in figure 9a, where for strong yet unstratified fronts, the non-traditional effects  
 515 have a uniform influence of increasing (decreasing) the growth rate by  $\sim 25\%$  when the  
 516 buoyancy gradient is north (south). This effect is much less pronounced with even a weak  
 517 stratification of  $Ri = 0.25$ , in agreement with Colin de Verdière (2012).

518 By changing the contours of absolute momentum (A 3), the non-traditional Coriolis  
 519 terms also influence the angle of the SI modes. As shown in figure 9b, the SI mode angle  
 520 becomes steeper with increasing  $\gamma$ , and tends to align more with isopycnals as the tilted  
 521 rotation vector steepens the absolute momentum contours.

522 We finally consider how the energy source for SI changes with varying  $\gamma$ . This is best  
 523 seen by the generalised production ratio (B 13) which is plotted for  $\gamma = \pm 1$  in figure 10.  
 524 Compared to figure 7b under the traditional approximation, we note similarly distinct  
 525 regions of slantwise convection (black) and slantwise inertial instability (red). These  
 526 regions are largely unchanged for large  $\Gamma$  (where the strong thermal wind shear means  
 527 that all rotation is less important), and the slantwise convective character still persists  
 528 near  $Ri = 1$  compared to the slantwise inertial instability region for small  $Ri$ . Still, the  
 529 energy source for weaker fronts appears to be influenced more by the non-traditional  
 530 effects.

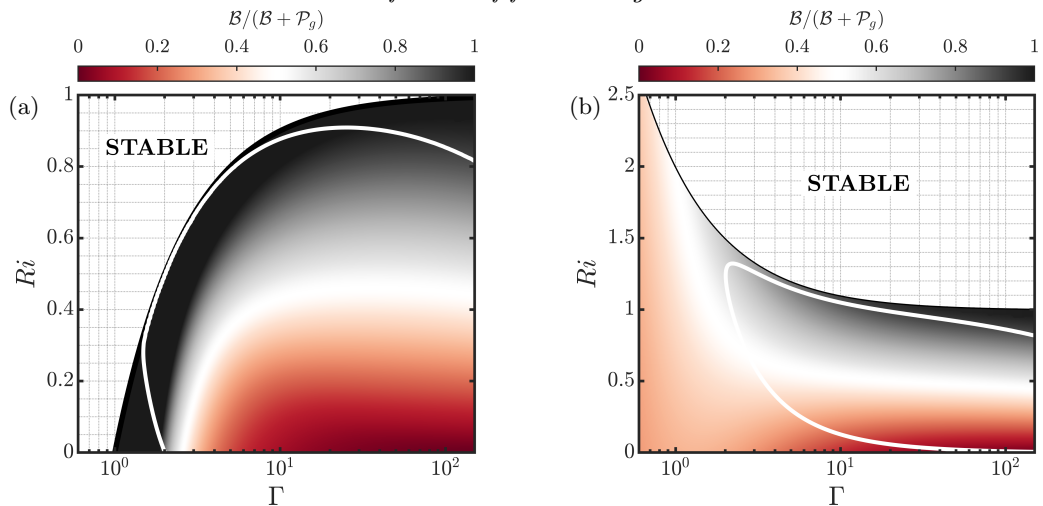


FIGURE 10. Contours of the production ratio (B 13) for (a)  $\gamma = 1$  and (b)  $\gamma = -1$ . (Note the different  $y$ -axis scales.) This metric in  $Ri$ - $\Gamma$  parameter space distinguishes regions where geostrophic shear production dominates (0) and regions that buoyancy production dominates (1), as shown in figure 7b in the traditional approximation. The black solid line is the sub-critical Richardson number,  $Ri_c = 1 - \gamma/\Gamma$ , which is no longer equal to 1. The white line separates regions of parameter space where SI modes are aligned closer to isopycnals (inside) from regions (outside) where they are more along absolute momentum surfaces. Comparing these two contour plots with figure 7b shows similarly distinct regions that could be characterised as ‘slantwise convection’ separated from the ‘slantwise inertial instability.’

## Appendix B. Primary linear stability analysis

### B.1. Symmetric instability eigenfunctions

Following the linear stability analysis of §2.2, but using the new momentum equation (A 1) containing the non-traditional Coriolis terms, then equation (2.10) instead becomes

$$\left[ \left( i\omega - \frac{k_x^2 + k_z^2}{Re} \right)^2 + \frac{1}{\Gamma^2} \right] D^2 \hat{\psi} + \frac{2ik_x}{\Gamma} \left( 1 - \frac{\gamma}{\Gamma} \right) D \hat{\psi} - k_x^2 \left[ \left( i\omega - \frac{k_x^2 + k_z^2}{Re} \right)^2 - \frac{\gamma}{\Gamma} \left( 1 - \frac{\gamma}{\Gamma} \right) + Ri \right] \hat{\psi} = 0. \quad (\text{B } 1)$$

This ODE is reduced to a quadratic eigenproblem by noting that solutions have the general form,

$$\hat{\psi} = \exp(i\lambda_1 z) - \exp(i\lambda_2 z) \quad (\text{B } 2)$$

which satisfy the boundary conditions (2.8) if

$$\lambda_1 - \lambda_2 = 2\pi n. \quad (\text{B } 3)$$

$\lambda_1$  and  $\lambda_2$  are then just the quadratic roots,

$$\lambda_{1,2} = \frac{-b \pm \sqrt{b^2 - 4ac}}{2a}, \quad (\text{B } 4)$$

where

$$a = - \left[ \left( i\omega - \frac{1}{Re} (k_x^2 + k_z^2) \right)^2 + \frac{1}{\Gamma^2} \right] \quad (\text{B } 5a)$$

$$b = \frac{2k_x}{\Gamma} \left( 1 - \frac{\gamma}{\Gamma} \right) \quad (\text{B } 5b)$$

$$c = -k_x^2 \left( \left( i\omega - \frac{1}{Re} (k_x^2 + k_z^2) \right)^2 - \frac{\gamma}{\Gamma} \left( 1 - \frac{\gamma}{\Gamma} \right) + Ri \right). \quad (\text{B } 5c)$$

537 The final constraint is given by the vertical viscous wave-mode approximation,

$$k_z^2 = \frac{1}{2} (\lambda_1^2 + \lambda_2^2). \quad (\text{B } 6)$$

This system of algebraic equations (B 3 - B 6) implicitly defines  $\omega$  as a function of  $k_x$ , and is solved by numerical iteration to construct the growth curve, as in figure 2a. For SI, the real part of the frequency is 0, i.e.  $\Re(\omega) = 0$ , and so then computing  $\lambda_1$  and  $\lambda_2$  gives the vertical structure for the eigenmodes:

$$\hat{u} = - \frac{1}{|\hat{U}|} (\lambda_1 \exp(iz\lambda_1) - \lambda_2 \exp(iz\lambda_2)) \quad (\text{B } 7a)$$

$$\hat{v} = - \frac{1}{|\hat{U}|} \frac{(k_x(\Gamma - \gamma) - \lambda_1) \exp(iz\lambda_1) - (k_x(\Gamma - \gamma) - \lambda_2) \exp(iz\lambda_2)}{\Gamma((k_x^2 + k_z^2)/Re + \sigma)} \quad (\text{B } 7b)$$

$$\hat{w} = \frac{1}{|\hat{U}|} k_x (\exp(iz\lambda_1) - \exp(iz\lambda_2)) \quad (\text{B } 7c)$$

$$\hat{b} = \frac{1}{|\hat{U}|} \frac{\lambda_1 \exp(iz\lambda_1) - \lambda_2 \exp(iz\lambda_2)}{\Gamma((k_x^2 + k_z^2)/Re + \sigma)}, \quad (\text{B } 7d)$$

538 where each component is normalised by the eigenmode velocity magnitude in the  $x$ - $z$   
539 plane,  $|\hat{U}| \equiv \sqrt{|\hat{u}|^2 + |\hat{w}|^2}$ . The full structure and evolution of the linear perturbations  
540 is then

$$u'(x, z, t) = \Re \left[ \hat{u}(z) e^{i(k_x x - \omega t)} \right] \quad (\text{B } 8)$$

541 and correspondingly for each of the other components.

542 We can now compute the angle of the SI modes,  $\theta$ , from the horizontal by analysing  
543 the zero-contours of

$$\psi(x, z) = \Re \left[ \hat{\psi}(z) e^{ik_x x} \right]. \quad (\text{B } 9)$$

544 The slope of these contours is

$$\frac{dz}{dx} = \frac{-2k_x}{\lambda_1 + \lambda_2} = \frac{a\Gamma}{1 - \gamma/\Gamma}, \quad (\text{B } 10)$$

545 and so  $\theta = \tan^{-1}(a\Gamma/(1 - \gamma/\Gamma))$ , for  $a$  from equation (B 5a). It is thus apparent that  $\theta$  in  
546 this vertical viscous wave-mode approximation is independent of height. The exact linear  
547 mode angle computed using a pseudo-spectral eigenvalue solver shows that the actual  
548 angle is in fact a very weak function of  $z$ , decreasing by at most 5% near the boundaries  
549 at the extremes of our parameter space. It should also be noted that while figure 7 shows  
550 the diagnostics of the dominant (fastest growing) SI mode, there is still a distribution of  
551 slower SI modes with varying characteristics.

## B.2. Symmetric instability energetics

552

Using the above eigenfunctions (B7), we can write the geostrophic shear production generated by the SI modes in terms of the growing mode amplitude,  $U_{\text{SI}}(t)$ :

553

554

$$\mathcal{P}_g = - \left\langle \frac{\overline{v'w'}}{v'w'} \frac{\partial \bar{v}_g}{\partial z} \right\rangle = - \frac{U^2}{|\hat{U}|^2} \frac{k_x}{2\Gamma} \frac{\lambda_1 + \lambda_2 - 2k_x(\Gamma - \gamma)}{(k_x^2 + k_z^2)/Re + \sigma}. \quad (\text{B } 11)$$

All of the time-dependence of  $\mathcal{P}_g$  is contained in  $U_{\text{SI}}(t)$ . Therefore when considering the production at  $\tau_c$  (as in §4) this expression is correspondingly scaled by  $U_{\text{SI}}(\tau_c)^2 = U_c^2$  (as computed in appendix C and plotted in figure 5a). The buoyancy production is similarly computed as

555

556

557

558

$$\mathcal{B} = \langle \overline{w'b'} \rangle = \frac{U_{\text{SI}}^2}{|\hat{U}|^2} \frac{k_x}{2\Gamma} \frac{\lambda_1 + \lambda_2}{(k_x^2 + k_z^2)/Re + \sigma}. \quad (\text{B } 12)$$

The fraction of the total production contributed by buoyancy can then be simplified as

559

$$\frac{\mathcal{B}}{\mathcal{B} + \mathcal{P}_g} = \frac{\lambda_1 + \lambda_2}{2k_x\Gamma} = \frac{-1}{a\Gamma(\Gamma - \gamma)} \quad (\text{B } 13)$$

for  $a$  from equation (B5a).

560

## B.3. Symmetric instability transport

561

The dominant balance of the  $y$ -momentum equation during the initial phase of adjustment as SI is mixing down the thermal wind shear is given by

562

563

$$\partial_t \bar{v} \approx -\partial_z \overline{v'w'} \quad (\text{B } 14)$$

as shown in §5. It is straightforward to determine the contribution of the SI modes to the evolution of the vertical shear,  $\partial_z \bar{v}$ :

564

565

$$\left\langle \frac{\partial^2 \overline{v'w'}}{\partial z^2} \right\rangle = \frac{U_{\text{SI}}^2}{|\hat{U}|^2} \frac{4\pi n^2 k_x}{\Gamma} \frac{\lambda_1 + \lambda_2 - 2k_x(\Gamma - \gamma)}{(k_x^2 + k_z^2)/Re + \sigma} \quad (\text{B } 15)$$

again using the normalised eigenfunctions (B7) and scaling by  $U_{\text{SI}}^2$  to correspond to the time when the SI mode has amplitude  $U_{\text{SI}}$ . We can then construct a thermal wind shear mixing time-scale using the instantaneous mixing rate (B15) evaluated at  $\tau_c$ :

$$\begin{aligned} \tau_{\text{mix}} f &= f \frac{\partial \bar{v}_g}{\partial z} \left\langle \frac{\partial^2 \overline{v'w'}}{\partial z^2} \right\rangle_c^{-1} \\ &= \frac{|\hat{U}|^2}{U_c^2} \frac{1}{4\pi n^2 k_x} \frac{(k_x^2 + k_z^2)/Re + \sigma}{\lambda_1 + \lambda_2 - 2k_x(\Gamma - \gamma)} \end{aligned} \quad (\text{B } 16)$$

using the critical mode amplitude,  $U_c$ , calculated in appendix C. This time-scale is plotted in figure 8a. Rather time-integrating the mixing rate through  $\tau_c$ , then we get a measure for the cumulative contribution of the SI modes to mixing down the thermal wind shear:

566

567

568

$$\int_0^{\tau_c} \left\langle \frac{\partial^2 \overline{v'w'}}{\partial z^2} \right\rangle dt = \frac{1}{2\sigma} \frac{U_c^2}{|\hat{U}|^2} \left\langle \frac{\partial^2 \overline{v'w'}}{\partial z^2} \right\rangle, \quad (\text{B } 17)$$

using the SI mode mixing rate from equation (B15). We consider  $U_{\text{SI}}$  at  $t = 0$  to be infinitesimal so that the lower limit of integration evaluates to 0. In the dimensionless units used throughout this paper ( $M^2/f$ ), this quantity represents the fraction of the thermal wind shear which is destroyed by  $\tau_c$  (i.e.  $1 - s$ ), and is plotted in figure 8b.

569

570

571

572

### 573 Appendix C. Secondary linear stability calculation

We conduct a secondary linear stability analysis to determine the time at which the growing SI modes break down and prompt transition to turbulence. We consider perturbations to the basic state shown in figure 4, which includes both the Eady basic state for the primary linear stability analysis superimposed with the fastest growing SI mode of amplitude,  $U_{\text{SI}}$ . This dimensionless basic state is

$$\bar{u} = U_{\text{SI}} \Re[\hat{u}(z) \exp(ik_x x)] \quad (\text{C } 1a)$$

$$\bar{v} = U_{\text{SI}} \Re[\hat{v}(z) \exp(ik_x x)] + z \quad (\text{C } 1b)$$

$$\bar{w} = U_{\text{SI}} \Re[\hat{w}(z) \exp(ik_x x)] \quad (\text{C } 1c)$$

$$\bar{b} = U_{\text{SI}} \Re[\hat{b}(z) \exp(ik_x x)] + \Gamma^{-1}x + Ri z, \quad (\text{C } 1d)$$

again using the normalised SI eigenfunctions (B 7). The analysis is greatly simplified by rotating the domain by  $\theta$  to align with the SI modes as evaluated at the mid-plane, such that the transformed coordinate  $x^\dagger$  is along SI modes and  $z^\dagger$  is perpendicularly across modes. The  $w^{\dagger}$  component of the eigenfunction at  $z = 1/2$  then becomes 0. Focusing on shear instability at the mid-plane, we extend the eigenmodes as sinusoids with the inclination and perpendicular wavenumber,  $k_{\text{SI}} \equiv |\mathbf{k}_{\text{SI}}| = \sqrt{k_x^2 + k_z^2}$ , evaluated at  $z = 1/2$  such that  $\theta = \sin^{-1}(k_x/k_{\text{SI}})$ . This new rotated basic state is then

$$\bar{u}^\dagger = U_{\text{SI}} \sin(k_{\text{SI}} z^\dagger) \quad (\text{C } 2a)$$

$$\bar{v}^\dagger = -U_{\text{SI}} \frac{\Gamma^{-1} \cos \theta - (1 - \gamma/\Gamma) \sin \theta}{\sigma + k_{\text{SI}}^2/Re} \sin(k_{\text{SI}} z^\dagger) + (z^\dagger \cos \theta - x^\dagger \sin \theta) \quad (\text{C } 2b)$$

$$\bar{b}^\dagger = -U_{\text{SI}} \frac{\Gamma^{-1} \cos \theta}{\sigma + k_{\text{SI}}^2/Re} \sin(k_{\text{SI}} z^\dagger) + \Gamma^{-1} (z^\dagger \sin \theta + x^\dagger \cos \theta) + Ri (z^\dagger \cos \theta - x^\dagger \sin \theta). \quad (\text{C } 2c)$$

We note that this basic state now has a background stratification with a component induced by the SI modes. Similarly rotating the governing equations (2.2) and linearising about this new basic state, then the linearised system becomes

$$\begin{aligned} \partial_t u' + \bar{u}^\dagger \partial_x u' + w' \partial_z \bar{u}^\dagger &= -\partial_x \Pi' + \frac{1}{\Gamma} v' (\cos \theta + \gamma \sin \theta) + \frac{1}{Re} \nabla^2 u' - b' \sin \theta \\ \partial_t v' + \bar{u}^\dagger \partial_x v' + u' \partial_x \bar{v}^\dagger + w' \partial_z \bar{v}^\dagger &= -\frac{1}{\Gamma} [u' (\cos \theta + \gamma \sin \theta) + w' (\sin \theta + \gamma \cos \theta)] + \frac{1}{Re} \nabla^2 v' \\ \partial_t w' + \bar{u}^\dagger \partial_x w' &= -\partial_z \Pi' + \frac{1}{\Gamma} v' (\sin \theta + \gamma \cos \theta) + \frac{1}{Re} \nabla^2 w' + b' \cos \theta \\ \partial_t b' + u' \partial_x \bar{b}^\dagger + \bar{u}^\dagger \partial_x b' + w' \partial_z \bar{b}^\dagger &= \frac{1}{Re} \nabla^2 b' \\ 0 &= \nabla \cdot \mathbf{u}' \end{aligned} \quad (\text{C } 3)$$

574 where all perturbation quantities and derivatives are relative to the rotated coordinates.  
 575 For large  $\Gamma$ , we can ignore the effects of rotation on the secondary instability. If we  
 576 also for a moment ignore the  $x^\dagger$  component of the background stratification, then  
 577 this system reduces to the Taylor–Goldstein equation and can be easily numerically  
 578 solved for  $\sigma_{\text{KH}}(k_{\text{KH}})$  for each SI mode amplitude,  $U_{\text{SI}}$ . We designate SI criticality when  
 579  $\sigma_{\text{KH,max}} = \sigma_{\text{SI}}$ , and so for each  $\Gamma$  we compute the required critical mode amplitude,  $U_c$ ,  
 580 when this condition is met. This classical KHI solution is plotted with a grey dotted  
 581 line in figure 5a. Accounting now for rotation effects and also the full SI mode buoyancy

582 contribution, then the system (C3) can only be reduced to a system of three equations  
 583 for  $\psi'$ ,  $v'$ , and  $b'$ , which have a normal mode form  $\xi(x^\dagger, z^\dagger, t) = \hat{\xi}(z^\dagger) \exp(i(k_{\text{KH}}x^\dagger - \omega t))$ .  
 584 We numerically solve this system for each  $\sigma_{\text{KH}}(k_{\text{KH}}; U_{\text{SI}})$  using a 1D pseudo-spectral  
 585 eigenvalue solver written in `Matlab`, and using  $N = 128$  Fourier modes across a width of  
 586  $2\lambda_{\text{SI}}$ . We solve the nonlinear optimisation problem to find the minimum  $U_{\text{SI}}$  that satisfies  
 587  $\sigma_{\text{KH}}(k_{\text{KH}}; U_{\text{SI}}) = \sigma_{\text{SI}}$ , and plot this  $U_c(I)$  as a solid line in figure 5a. This value for  $U_c$   
 588 can then be used to calculate the various transport and energetic quantities for SI in  
 589 appendix B.

## REFERENCES

- 590 BACHMAN, S D, FOX-KEMPER, B, TAYLOR, J R & THOMAS, L N 2017 Parameterization of  
 591 Frontal Symmetric Instabilities. I: Theory for Resolved Fronts. *Ocean Modelling* **109**,  
 592 72–95.
- 593 BACHMAN, S. D. & TAYLOR, J. R. 2014 Modelling of partially-resolved oceanic symmetric  
 594 instability. *Ocean Modelling* **82**, 15–27.
- 595 BOCCALETTI, GIULIO, FERRARI, RAFFAELE & FOX-KEMPER, BAYLOR 2007 Mixed layer  
 596 instabilities and restratification. *Journal of Physical Oceanography* **37** (9), 2228–2250.
- 597 CALLIES, JÖRN, FLIERL, GLENN, FERRARI, RAFFAELE & FOX-KEMPER, BAYLOR 2016 The role  
 598 of mixed-layer instabilities in submesoscale turbulence. *Journal of Fluid Mechanics* **788**,  
 599 5–41.
- 600 CHARNEY, J. G. 1947 The Dynamics of Long Waves in a Baroclinic Westerly Current. *Journal*  
 601 *of Meteorology* **4** (5), 136–162.
- 602 COLIN DE VERDIÈRE, ALAIN 2012 The stability of short symmetric internal waves on sloping  
 603 fronts: Beyond the traditional approximation. *Journal of Physical Oceanography* **42** (3),  
 604 459–475.
- 605 D’ASARO, ERIC A., LEE, CRAIG M., RAINVILLE, LUC, HARCOURT, RAMSEY & THOMAS,  
 606 LEIF N. 2011 Enhanced turbulence and energy dissipation at ocean fronts. *Science*  
 607 **332** (6027), 318–322.
- 608 EADY, E. T. 1949 Long Waves and Cyclone Waves. *Tellus* **1** (3), 33–52.
- 609 FOX-KEMPER, BAYLOR, FERRARI, RAFFAELE & HALLBERG, ROBERT 2008 Parameterization  
 610 of mixed layer eddies. part i: Theory and diagnosis. *Journal of Physical Oceanography*  
 611 **38** (6), 1145–1165.
- 612 GRISOUARD, NICOLAS 2018 Extraction of Potential Energy from Geostrophic Fronts by  
 613 Inertial–Symmetric Instabilities. *Journal of Physical Oceanography* **48** (5), 1033–1051.
- 614 GRISOUARD, NICOLAS & THOMAS, LEIF N 2016 Energy exchanges between density fronts and  
 615 near-inertial waves reflecting off the ocean surface. *Journal of Physical Oceanography*  
 616 **46** (2), 501–516.
- 617 HAINE, THOMAS W.N. & MARSHALL, JOHN 1998 Gravitational, symmetric, and baroclinic  
 618 instability of the ocean mixed layer. *Journal of Physical Oceanography* **28** (4), 634–658.
- 619 HOSKINS, B. J. 1974 The role of potential vorticity in symmetric stability and instability.  
 620 *Quarterly Journal of the Royal Meteorological Society* **100** (425), 480–482.
- 621 HOSKINS, B. J. & BRETHERTON, F. P. 1972 Atmospheric Frontogenesis Models: Mathematical  
 622 Formulation and Solution. *Journal of the Atmospheric Sciences* **29** (1), 11–37.
- 623 JINADASA, S. U. P., LOZOVATSKY, LOSSIF, PLANELLA-MORATÓ, JESUS, NASH, JONATHAN,  
 624 MACKINNON, JENNIFER, LUCAS, ANDREW, WIJESEKERA, HEMANTHA & FERNANDO,  
 625 HARINDA 2016 Ocean Turbulence and Mixing Around Sri Lanka and in Adjacent Waters  
 626 of the Northern Bay of Bengal. *Oceanography* **29** (2), 170–179.
- 627 SARKAR, SUTANU, PHAM, HIEU T, RAMACHANDRAN, SANJIV, NASH, JONATHAN D, TANDON,  
 628 AMIT, BUCKLEY, JARED, LOTLIKER, ANEESH A & OMAND, MELISSA M 2016 The  
 629 interplay between submesoscale instabilities and turbulence in the surface layer of the  
 630 bay of bengal. *Oceanography* **29** (2), 146–157.
- 631 SAVELYEV, I., THOMAS, LEIF N., SMITH, G. B., WANG, Q., SHEARMAN, R. K., HAACK,  
 632 T., CHRISTMAN, A. J., BLUMQUIST, B., SLETTEN, M., MILLER, W. D. & FERNANDO,  
 633 HARINDA 2018 Aerial Observations of Symmetric Instability at the North Wall of the Gulf  
 634 Stream. *Geophysical Research Letters* **45** (1), 236–244.

- 635 STAMPER, MEGAN A. & TAYLOR, JOHN R. 2016 The transition from symmetric to baroclinic  
636 instability in the Eady model. *Ocean Dynamics* **67** (1), 65–80.
- 637 STONE, PETER H. 1966 On Non-Geostrophic Baroclinic Stability. *Journal of the Atmospheric*  
638 *Sciences* **23** (4), 390–400.
- 639 STONE, PETER H. 1970 On Non-Geostrophic Baroclinic Stability: Part II. *Journal of the*  
640 *Atmospheric Sciences* **27** (5), 721–726.
- 641 STONE, PETER H. 1971 Baroclinic stability under non-hydrostatic conditions. *Journal of Fluid*  
642 *Mechanics* **45** (4), 659–671.
- 643 STONE, PETER H. 1972 On non-geostrophic baroclinic stability: Part iii. the momentum and  
644 heat transports. *Journal of the Atmospheric Sciences* **29** (3), 419–426.
- 645 TANDON, AMIT & GARRETT, CHRIS 1994 Mixed layer restratification due to a horizontal density  
646 gradient. *Journal of Physical Oceanography* **24** (6), 1419–1424.
- 647 TAYLOR, JOHN R. 2008 Numerical Simulations of the Stratified Oceanic Bottom Boundary  
648 Layer. PhD thesis, University of California, San Diego.
- 649 TAYLOR, JOHN R. & FERRARI, RAFFAELE 2009 On the equilibration of a symmetrically unstable  
650 front via a secondary shear instability. *Journal of Fluid Mechanics* **622**, 103–113.
- 651 TAYLOR, JOHN R. & FERRARI, RAFFAELE 2010 Buoyancy and wind-driven convection at mixed  
652 layer density fronts. *Journal of Physical Oceanography* **40** (6), 1222–1242.
- 653 THOMAS, LEIF N. & LEE, CRAIG M. 2005 Intensification of ocean fronts by down-front winds.  
654 *Journal of Physical Oceanography* **35** (6), 1086–1102.
- 655 THOMAS, LEIF N. & TAYLOR, JOHN R. 2010 Reduction of the usable wind-work on the general  
656 circulation by forced symmetric instability. *Geophysical Research Letters* **37** (18).
- 657 THOMAS, LEIF N., TAYLOR, JOHN R., D’ASARO, ERIC A., LEE, CRAIG M., KLYMAK, JODY M.  
658 & SHCHERBINA, ANDREY 2016 Symmetric instability, inertial oscillations, and turbulence  
659 at the gulf stream front. *Journal of Physical Oceanography* **46** (1), 197–217.
- 660 THOMAS, LEIF N., TAYLOR, JOHN R., FERRARI, RAFFAELE & JOYCE, TERRENCE M. 2013  
661 Symmetric instability in the Gulf Stream. *Deep-Sea Research Part II: Topical Studies in*  
662 *Oceanography* **91** (C), 96–110.
- 663 THOMPSON, ANDREW F., LAZAR, AYAH, BUCKINGHAM, CHRISTIAN, GARABATO, AL-  
664 BERTO C. NAVEIRA, DAMERELL, GILLIAN M. & HEYWOOD, KAREN J. 2016a Open-ocean  
665 submesoscale motions: A full seasonal cycle of mixed layer instabilities from gliders.  
666 *Journal of Physical Oceanography* **46** (4), 1285–1307.
- 667 THOMPSON, ANDREW F., LAZAR, AYAH, BUCKINGHAM, CHRISTIAN, NAVEIRA GARABATO,  
668 ALBERTO C., DAMERELL, GILLIAN M. & HEYWOOD, KAREN J. 2016b Open-ocean  
669 submesoscale motions: A full seasonal cycle of mixed layer instabilities from gliders.  
670 *Journal of Physical Oceanography* **46** (4), 1285–1307.
- 671 WANG, PENG, MCWILLIAMS, JAMES C & MÉNESGUEN, CLAIRE 2014 Ageostrophic instability in  
672 rotating, stratified interior vertical shear flows. *Journal of fluid mechanics* **755**, 397–428.
- 673 WEBER, JAN E 1980 Symmetric instability of stratified geostrophic flow. *Tellus* **32** (2), 176–185.
- 674 YU, XIAOLONG, NAVEIRA GARABATO, ALBERTO C., MARTIN, ADRIAN P., GWYN EVANS, D.  
675 & SU, ZHAN 2019 Wind-Forced Symmetric Instability at a Transient Mid-Ocean Front.  
676 *Geophysical Research Letters* **46** (20), 11281–11291.
- 677 ZEITLIN, V. 2018 Letter: Symmetric instability drastically changes upon inclusion of the full  
678 Coriolis force. *Physics of Fluids* **30** (6).